SUPPLEMENTAL INFORMATION

Negatively charged lipid membranes promote a disorder-order transition in the Yersinia YscU Protein

Christoph F. Weise[‡1], Frédéric H. Login[§], Oanh Ho[‡], Gerhard Gröbner[‡], Hans Wolf-Watz[§] and Magnus Wolf-Watz[‡2]

[‡]Department of Chemistry, Chemical Biological Center, Umeå University, SE- 901 87 Umeå, Sweden

[§] Department of Molecular Biology and The Laboratory for Molecular Infection Medicine Sweden (MIMS), Umeå Centre for Microbial Research (UCMR), Umeå University, SE-901 87 Umeå, Sweden

SUPPLEMENTAL EXPERIMENTAL PROCEDURES

Structure calculation from NMR restraints with XPLOR-NIH

NOEs, chemical shifts and $^{3}J_{HNHA}$ couplings were combined as restraints during generation of a conformational ensemble by implementing simulated annealing and molecular dynamics with the XPLOR-NIH package (vs. 2.33) (1, 2). Supplementary Table S1 summarizes the number of NMR restraints (300 total) collected, according to type. NOE restraint tables were generated with the program Ansig for windows (3) from a 3D NOESY spectrum. Crosspeak volumes were normalized to the mean value and classified as weak if I<0.87, intermediate if 0.87<I<5 and strong if I>5. A quadratic distance restraint potential was implemented with a lower bound of 1.8 Å and the following upper bounds: weak, r_{upper} = 6.0 Å; intermediate, r_{upper} = 3.6 Å; strong, r_{upper} = 2.7 Å. Chemical shifts ($^{1}H^{\alpha}$, $^{1}H^{N}$, $^{13}C^{\alpha}$ and ^{15}N) were converted into dihedral restraints using TALOS+ (4). Dihedral angles classified as ambiguous or highly dynamic by TALOS+ were excluded. $^{3}J_{HNHA}$ coupling restraints were implemented with a J-coupling potential using the following Karplus parameters: A=6.98, B=-1.38, and C=1.72, and a minimum uncertainty in ^{3}J of 0.5 Hz. Database or covalent restraints were implemented for bond lengths, angles, dihedrals, van der Waals contacts and hydrogen bonds. A mean-field database-derived Ramachandran torsion angle potential was employed to maintain backbone dihedral angles within favored regions for residues lacking sufficient restraints, particularly at the termini and interhelical regions (residues <212, >252, 229-233). Initial conformations were generated by imposing backbone dihedral angles corresponding to the TALOS+ restraints on a randomized conformation. The initial simulated annealing protocol consisted of high temperature dynamics for 800 ps at 3500 K followed by slow

cooling to 25 K in 12.5 K, 0.2 ps steps while switching on the NMR restraints. This was followed by energy minimizations in torsion-angle and then Cartesian space. The annealing/minimization cycles were iterated to generate 100 initial structures. Of these, the 20 lowest in energy satisfying the NMR restraints and PROCHECK criteria were selected (5). The preference of each residue for different secondary structure conformations was computed with program DSSP (6). by averaging over the ensemble of NMR structures. The limits of individual helices were defined for use in computation of charges, hydrophobicities (7)) and hydrophobic moments (8) from the DSSP averages using a value of 0.75 as the minimum helical population defining a residue as part of a helix.

NMR spin relaxation

Backbone amide ^{15}N R_1, R_2 and ^{15}N-^{1}H NOE measurements were performed with phase-sensitive gradient-enhanced ^{15}N-^{1}H PEP-HSQC pulse programs with flip-back pulses and GARP decoupling during acquisition (9). R_1 data was acquired with DIPSI2 ^{1}H decoupling during relaxation delays of 0.100, 0.150, 0.250, 0.370, 0.510 0.825, 1.05, and 1.50 s. For R_2 experiments relaxation delays of 17, 52, 86, 138, 173, 242, 294 and 346 ms were used. ^{15}N-^{1}H NOE spectra were acquired in an interleaved manner, with a 5 s relaxation delay and a 3 s NOE buildup period. Relaxation rates R_1 and R_2 were derived from non-linear least-squares fits (Levenberg-Marquardt algorithm) with single exponential functions, $I[t] = I[0] \exp(-t R_{1/2})$, with t the relaxation delay and I[t] the crosspeak volume. Uncertainties in the $R_{1,2}$ relaxation parameters were derived from the parameter covariance matrix combined with uncertainties in integrated crosspeak

volumes estimated from the baseline RMS noise level. Uncertainties in the NOEs were derived from the RMS baseline noise and crosspeak volumes. Complete relaxation data was obtained for 41 of 52 $YscU_{CN}$ residues unaffected by resonance overlap as well as 3 residues from the construct linker (Fig. S2). For NMR relaxation measurements and other HSQC-based experiments, resonance overlap interfered with quantification for the following residues at pH 6.0: K212, E213, K215, K222, K237, R239, Q240, I245, E252, K255, and V260.

pH Perturbation

As an additional probe of solvent exposure, the effect of a pH perturbation on chemical shifts was monitored by acquiring ^{1}H-^{15}N HSQC spectra at pH 6.0 and 7.0. Water was employed as an internal reference using the known dependence of its chemical shift on pH and temperature. The chemical shift response $\Delta\delta$ of backbone amide $^{1}H^{N}$ and ^{15}N with the pH change were used to compute a mean response according to Equation S1:

$$\delta_{avg} = [\Delta\delta_H^2 + (0.15\Delta\delta_N)^2]^{1/2} \qquad \textbf{(Equation S1)}$$

Amide Exchange Measurements

Exchange of protein amide protons (H^N) with water was monitored by NMR to discriminate shielded from solvent accessible regions of the backbone amide groups. The CLEANEX-PM-FHSQC experiment was employed to measure the exchange rate k_{ex} under fast exchange conditions ($k_{ex}>1\ s^{-1}$) (10). CLEANEX-PM mixing delays of 100 ms and 300 ms were applied. Crosspeak volumes in the exchange spectra were normalized

to integrals from a reference FHSQC spectrum (11). Residues I221, E233, M250 and V259 with strongly overlapping HSQC crosspeaks were excluded from the analysis.

The exchange buildup curves were fit with Equation 1 from Ref. ((10)) to derive k_{ex}. The buildup process is determined by k_{ex} and by the relaxation rates of amide and solvent magnetizations. The effective relaxation rate of water, a uniformly valued (global) parameter in all of the fits, was fixed at a value of 0.6 s^{-1} based on an independent measurement (10). Lower and upper bounds for the relaxation rate R_{1A} of 0.01 s^{-1} and 50 s^{-1} were selected based on $^1H^N$ R_1 and R_2 rates estimated from the global correlation time of the micellar aggregate and a dipolar interaction with a minimum interproton distance of 2 Å. Solvent protection factors $P_{solv}=k_{rc}/k_{prot}$ were computed from reference random coil exchange rates k_{rc} obtained with the program SPHERE (http://www.fccc.edu/research/labs/roder/sphere) using the standard parameter set for poly-DL-alanine (12) (13) and activation energies derived from the high-temperature behavior of BPTI and Ribonuclease A. Large uncertainties ($\sigma_s \approx k_{ex}$) in fitted parameters and computed protection factors were obtained for residues I211, L214, R223, K226, E244, and I245. For these residues the large uncertainty is due to a small signal buildup attributed to a small k_{ex} (<0.4 s^{-1}) and associated large protection factor ($k_{rc} >> k_{ex}$).

SUPPLEMENTAL RESULTS AND DISCUSSION

Structure Prediction from NOEs, Chemical Shifts, and $^3J_{HNHA}$ Couplings

The $^3J_{HNHA}$ spin-spin coupling constant is diagnostic of the value of the backbone dihedral angle ϕ: $^3J_{HNHA}$ <6 Hz is indicative of α-helical structure while $^3J_{HNHA}$>8 Hz is consistent with extended conformations (14). Couplings were obtained for 34 of 55 backbone residues in SDS-complexed $YscU_{CN}$ (Fig. 5B). Most values for residues in the range D219-S258 are consistent with α-helical conformation. Exceptions occur at residues S217, E227, G230-S231 and N253, which display intermediate coupling magnitudes suggestive of large-amplitude conformational sampling. Couplings for residues above S257 and below residue I211 also lie near or above 6 Hz, pointing to the predominance of disordered conformations at the termini, and only residue N263 has a coupling strongly suggestive of an extended conformation.

Helical regions predicted from the input primary amino acid sequence and $^1H^{\alpha}$, $^1H^{N}$, $^{13}C^{\alpha}$ and ^{15}N chemical shifts by program MICS are overlayed in Fig. 5A onto deviations $\Delta\delta$ of $^{13}C^{\alpha}$ shifts from random coil values. The ordered regions predicted by MICS are almost exclusively helical. MICS identified three helical stretches of 5 or more residues and three 2-3 residue spans exhibiting helical character. The longer helical stretches G[-1]-K215, K218-M228, and E233-S247 coincide with regions exhibiting $^3J_{HNHA}$ and ^1H-^1H dipole coupling patterns characteristic of α-helical conformation. Negative $\Delta\delta$ $^{13}C^{\alpha}$ for S217 and particularly the large negative value (-2.0 Hz) for S231 point to an extended conformation. MICS suggested a cap structure for residue S217 as part of a helical N-capping motif (Q=0.89). Other notable structural motifs suggested by the primary sequence include a type-VI β-turn involving residues G230-E233 (MICS is not trained

for identification of this type of β-turn). The remaining residues are predicted to be within loops.

The helical stretches identified on the basis of NOEs, chemical shifts, and $^{3}J_{HNHA}$ agree well with the predictions of program PSI-PRED based on the primary sequence of $YscU_{CN}$ (15) (16) (Fig. S1). Both MICS and PSI-PRED make predictions based on prior knowledge in the form of experimental structure and/or chemical shift databases. The agreement between the helical regions identified in a membrane-mimicking environment and predictions based on a database of reported protein structures can reflect universal principles guiding helix formation. Minor differences do arise between the predictions of MICS versus PSI-PRED. For instance, the third helix predicted by PSI-PRED extends up to N253, further than S247 as suggested by MICS, incorporating the short helical stretch M250-E252 also identified by MICS. There remains some ambiguity with regard to the termination point of helix 3. It is perhaps no coincidence that crystal structures of different $YscU_{C}$ homologues provide mixed predictions on helical structure within the second half of $YscU_{CN}$ (residues > R239, see Fig. 1C).

Structure calculations

Supplementary Table S1 summarizes the validation results for the 20 low energy structures generated by imposing NMR restraints during XPLOR-NIH simulations of $YscU_{CN}$. Deviations between restraints and computed distances, dihedral angles and $^{3}J_{HNHA}$ couplings were generally small with only minor violations. Structure ensemble, restraints list and chemical shifts are available at the BMRB and RCSB data banks (BMRB ID 19809 and PDB ID 2ml9). Although structures with backbone dihedral angles

in Ramachandran regions labeled as unallowed by PROCHECK were excluded, the absence of NMR restraints in loop and terminal regions (<K212, >E252, G230-E233) led to a significant population of generously allowed backbone conformations (uncommonly observed in databases) among those residues. The reported backbone conformation of these loop and terminal residues is not meaningful insofar as they were not subject to NMR restraints but only depend on the intrinsic XPLOR-NIH potential terms. In addition, the ϕ/ψ dihedrals for residues M216-S217 and R248-N249, for which available NMR restraints were applied, were also prone to borderline values, which can be attributed to the labile nature of these regions at the interface with the disorganized loops/termini, and is reflected in the $^{13}C^{\alpha}$ chemical shifts and dihedral angles predicted by TALOS+ for those residues. Residues undergoing larger amplitude conformational exchange would be better described by ensemble simulations.

Residue-specific secondary structure conformational preferences computed with program DSSP and averaged over the ensemble of NMR structures are displayed in Fig. 6A. The three stretches marked by high occupation (population>0.75) of α-helical conformations are clearly identified, spanning residues S[0]-K215, K218-E229, and I234-Q246. A shorter stretch involving M250-N253 exhibits a mixture of α-helical and primarily 3_{10} helical conformation. The helical stretches are in good agreement with the predictions provided by MICS on the basis of chemical shifts. The preservation of α-helical regions over the ensemble is shown in the close registry of backbones following alignment (Fig. 6B). Conformational variation in helix 2 is less than in helices 1 and 3 consistent with the greater number of NOE restraints observed in this region. The edges of helix 3 exhibit some variation (~20%) in the form of 3_{10} helical structures. Helix 1 also

shows heterogeneity including turn-like conformations particularly near helix 2. In addition, in ~33% of the structures the helical conformation extended between residues in helix 1 and 2, i.e. included M216 and S217.

NMR spin relaxation

Parameters describing global and residue-specific motions were derived from pooled ^{15}N R_1 and R_2 and ^{15}N-^{1}H NOE values (Fig. S2) for the 44 residues for which complete relaxation data was available, implementing a "modelfree" protocol similar to that outlined by Mandel *et al.* (17) with the program Dynamics (18-20). In the absence of a known structure for the protein fragment it was not possible to derive a full rotational diffusion tensor from the relaxation dataset alone. The global motion was therefore assumed to be described by an isotropic rotational tensor with a single correlation time τ_M. The assumption of isotropic motion is a reasonable first approximation consistent with the tendency of SDS to form spherical aggregates. The availability of data at only one magnetic field further constrained the choice of motional model to ones with three or less adjustable parameters. Standard models based on the model-free formalism of Lipari and Szabo (21, 22) were evaluated. In order of increasing complexity (number of fitting parameters), these are: LS model with very fast internal motions (τ_i 0, model 1); full LS model (model 2); fast LS model with a chemical exchange (R_{2ex}) contribution to R_2 ((23)); LS model with an R_{2ex} contribution (model 4); Clore's extended LS model with two timescales of internal motion (model 5 (23)). The parameters describing local motions are R_{2ex}, and the order parameter (S^2) and internal correlation time τ_i associated with the N-H bond vector. An appropriate value of the global correlation time was

selected using a grid search. During selection of a local motional model for each residue, local dynamic parameters were optimized *via* non-linear least-squares fits at preset values of the global correlation time on the τ_M grid. For each residue, an optimal model was selected based on two criteria: (1) a value of the goodness-of-fit sum-of-squares statistic χ^2_i within the 90% confidence interval; and (2) F-tests to compare alternative nested models, with rejection of the more complex model if the F-statistic falls within the 80% confidence interval. The performance of fits at different values of τ_M was assessed using the global sum-of-squares χ^2_{tot} and a reduced statistic $\chi^2_{red} = \chi^2_{tot}/n_{DF}$, where n_{DF} is the cumulative number of degrees of freedom. Uncertainties in the local motional parameters were estimated with the Monte Carlo approach implemented within Dynamics by fitting 500 mock data sets generated using the experimental data as template.

Internal and global dynamics from NMR relaxation data

Values of the global rotational correlation time τ_M and of local motional parameters S^2, τ_i, and R_{2ex} for SDS-associated $YscU_{CN}$ were derived from pooled ^{15}N R_1, R_2 and ^{15}N-^1H NOEs. The relaxation data analysis included residues >R251, <K218, and E229-K237, which undergo large amplitude internal motions as reflected by small ^{15}N-^1H NOEs (<0.55). The description of motions in these conformationally labile residues usually required use of 3-parameter models, particularly the Clore model but also the LS model incorporating a chemical exchange contribution. Fits involving 3-parameter models returned goodness-of-fit statistics $\chi^2_i \approx 0$, so dynamic residues described by these models did not contribute to the cumulative sum of χ^2_i over all residues (χ^2_{tot}). Of the 44 residues included in the relaxation analysis, only 13-18 within the comparatively rigid

helical regions and their boundaries contributed to χ^2_{tot}. For these residues in regions of low or intermediate mobility the choice of model often varied with τ_M without a significant effect on χ^2_i. Such compensatory effects complicated selection of the global correlation time τ_M since fits within the range 6 ns $<\tau_M<$8.3 ns satisfied the global goodness-of-fit condition $\chi^2_{tot} <\chi^2_{crit}$ (n_{DF}) and returned reasonable χ^2_i and physically meaningful local motional parameters for all residues. Various empirical criteria were therefore examined during selection of τ_M. These include monitoring changes in the choice of motional model along the primary sequence (18), the value of τ_M predicted by a trimmed R_2/R_1 analysis for residues undergoing fast internal motions, and reconciliation with the larger radius estimated from the translational diffusion coefficient (see below). These criteria resulted in selection of a τ_M value of 7.7 ns, which also corresponds to a local minimum in χ^2_{tot}, for computation of the reported internal motional parameters.

An independent estimate of τ_M=8.3±0.5 ns was obtained from the translational diffusion coefficient using Equations 2 and 3. The derived τ_M lies near the upper bound of the range of values deemed consistent with the relaxation data. Discrepancies between the values of τ_M suggested by the two techniques may be due to model approximations inherent in the SE and SED equations, particularly the assumption of sphericity. For particles of equal volume, deviations from a spherical particle shape increase D (24) . This explanation is viable as the diffusion measurement sampled two different conformations corresponding to the cis and trans amide isomers of Pro232, while the relaxation measurement focused on resonances assigned to the trans isomer and was less affected by conformational exchange. However, this hypothesis requires that the aspect ratio of the SDS complex formed by the cis species be much larger ($\Delta p>>1$) than that of

the *trans* conformer. Since this condition is unlikely to have been fulfilled, we favor other explanations. For instance, an alternative possibility for the comparatively short τ_M obtained from relaxation measurements is motion of the protein fragment *within* the SDS aggregate, which would effectively decouple the measured translational and rotational diffusion rates. This explanation is plausible given that the protein occupies only ~16% of the volume in the complex assuming typical values of the protein specific volume.

The pattern of the order parameters S^2 along the primary sequence is generally mirrored by structural evidence from ^{13}C chemical shifts, ^{1}H -^{1}H NOEs, and $^{3}J_{\alpha N}$ (Fig. S1). Residues K218-M228 and K235-S247 exhibit high order parameters (S^2>0.75) as well as $^{3}J_{\alpha N}$ couplings, NOEs and chemical shifts consistent with persistent helical structure. A greater rigidity of helix 2 compared to helix 3 is revealed in both higher order parameters and by a more dense pattern of long range NOEs for helix 2. On the other hand, the low order parameters *and* extensive pattern of NOEs in helix 1 (G[-1]-K215) might be better explained as the result of concerted motions of the entire helix relative to the remainder of the molecule. The abrupt discontinuity in S^2 at residues S217-K218 marks the position of a flexible joint between helices 1 and 2, while a broader cleft including residues E229-I234 marks the break between helices 2 and 3. Persistently high order parameters (S^2>0.7) hint at structure up to residue M250. Beyond this point evidence of structure may be inferred from other NMR parameters as far as residue V261, but not as clearly from S^2, which decreases rapidly and smoothly in value above M250.

The order parameters S^2_{RCI} computed with MICS from chemical shifts (Fig. 7) are overall in good agreement with S^2 derived from relaxation data, particularly for helix 2.

In other segments of the sequence S^2_{RCI} tends to be larger than S^2. Since high S^2_{RCI} generally reflects low conformational flexibility, the difference in the two order parameters is possibly due to rapid relative reorientations of helical segments. This is consistent with a short segment such as helix 1 reorienting rapidly relative to the other segments. Such reorientations can preserve the secondary structure within the segments and would thus not alter chemical shifts. S^2 is also slightly reduced in helix 3 compared to helix 2. The greater flexibility of helix 3 is consistent with exchange between α-helical and a small population of 3_{10} structures within the broader basin of helical conformations, as suggested by the NMR structural ensemble.

pH Perturbation

The effect of an increase in the solvent pH from 6.0 to 7.0 on backbone amide $^1H^N$ and ^{15}N chemical shifts for SDS-bound $YscU_{CN}$ (Fig. S3) served as an additional probe of the extent of solvent exposure of different residues in the protein. While free Glu and Asp sidechains in water at RT have an intrinsic acid dissociation constant in the range 3.5-4.5, acidic or basic residues (Glu, Asp, Lys, Arg and His) within helical peptides and proteins complexed with SDS can undergo pKa increases of ~1-2 units when localized within the environment created by proximal sulfate headgroups at the solvent interface (25) (26). The increase in pK_a translates into an enhanced chemical shift response of nearby nuclei, such as backbone amide $^1H^N$ and ^{15}N, when the pH is in the range 6-7, and explains the pH sensitivity of ^1H-^{15}N HSQC chemical shifts for residues in the second helix (residues K218-S231) and in the vicinity of H242 (residues R238-F241) within the $YscU_{CN}$-SDS

complex. The chemical shift response is significantly lower in the first helix, in the linker region involving residue P232, and for residues >M250, indicating that these segments are positioned away from the micellar interface. The response is also attenuated in the third helix, with a prominent local maximum in the response at H242.

Amide Exchange Measurements

Fast $^{1}H^{N}$ exchange rates determined with the CLEANEX-PM experiment and derived protection factors P_{solv} permit identification of solvent-exposed regions of the backbone and exchangeable sidechain protons (Fig. S4). Two principal mechanisms slow exchange in the SDS complex: burial in the interior of the complex, which shields exchangeable protons from the solvent, and the formation of long-lived intramolecular hydrogen bonds associated with secondary structure. The small protection factor (P_{solv}=3.3) of the N-terminal residue L[-2] is consistent with absence of secondary structure and high solvent exposure. P_{solv} in subsequent residues G[-1] to K215 is ~10-100× larger indicating burial within the complex or participation in the first alpha helix. Most residues in the Glu-rich region between E220 and S231 corresponding to helix 2 display intermediate protection factors (≈10) although basic residues R223 and K226 have larger P_{solv} which appears consistent with an amphipathic helix with alternating protected and exposed regions. The segment following P232 is more shielded with high protection factors exhibited around highly hydrophobic F241 within helix 3. There is a notable increase in exposure at Q246 marking the end of the third helix. Subsequent residues from M250 to S258 display a pattern of alternating large and small P_{solv}. Some evidence of secondary structure in that region comes from positive $\Delta\delta$ $^{13}C^{\alpha}$ chemical

shifts, suggesting the regularity in exposure may be due to helical structure. Rapid exchange rates of the C-terminal tail residues V261-N263 are consistent with solvent exposure and the absence of secondary structure, in agreement with the low order parameters derived from relaxation data and absence of other structural evidence, as well as a low D5S PRE for V261. The high solvent exposure of V259-V261 is somewhat surprising given the hydrophobic character of valine. These residues lack persistent secondary structure but may occupy interfacial positions with sidechains immersed in the micelle and the backbone accessible to water. In agreement with this location, weak ^{1}H-^{1}H NOESY crosspeaks were observed between water and $^{1}H^{N}$ of S258-A262. In summary, despite gaps in the sequential CLEANEX data, the pattern of exchange rates and protection factors is consistent with a positioning of the second amphipathic helix at an exposed interfacial position, significant burial of the C-terminal regions following P232 and particularly of the third helix, with a drop in solvent protection at the end of the third helix, and particularly for the terminal residues (>V259).

SUPPLEMENTAL TABLES

Table S1. Number of NMR restraints by type and violation statistics for NMR and geometric restraints computed for the final ensemble of 20 $YscU_{CN}$ structures generated with XPLOR-NIH and PROCHECK. [1]Ensemble average of the root-mean-squared deviation of restraint violations computed by XPLOR-NIH. [2]Standard deviation of the RMSD of the restraint violations, computed over the ensemble. [3]Average number of violations per structure as evaluated with the violation thresholds indicated in parentheses. [4]Dihedral angle restraints derived from chemical shifts with TALOS+.

NMR derived restraints	Number of restraints
Total distances (NOE)	203
Intraresidual distances (i=j)	39
Sequential distances (|i-j|=1	119
Short range distances (1<|i-j|<=4	45
Long range distances (|i-j|>4	0
Dihedral angle restraints[4]	80
J-coupling constant restraints	17

Restraint violations	RMSD[1] (SD[2])	Avg number of violations[3]
Bonds (Å)	0.002 (0.000)	0.0 (# viol. > 0.05 Å)
Angles (deg)	0.371 (0.010)	0.0 (# viol. > 5°)
Improper (deg)	0.272 (0.016)	0.0 (# viol. > 5°)
VDW (Å)		0.0 (# viol. > 0.2 Å)
NOE (Å)	0.013 (0.006)	0.0 (# viol. > 0.5 Å)
Dihedral angles[4] (deg)	0.134 (0.090)	0.0 (# viol. > 5°)
J-coupling constant (Hz)	0.392 (0.062)	0.0 (# viol. > 1 Hz)

Table S2: Bacterial strains and plasmids used in this study

Strains, plasmids, or constructs	Description[a]	Reference
E. coli strains		
BL21	IPTG-inducible T7 RNA polymerase	(27)
Top 10	Commercial one-shot competent cells	Invitrogen
Y. pseudotuberculosis strains		
YPIII(pIB102)	wild-type, parental strain, Km^r	
YPIII(pIB75)	*ysc*U null strain, $Km^{r\ r}$	(28)
Plasmids		
pGEX-6P3	Commercial vector with N-term. GST-fusion Cb^r	GE Healthcare
pBADmycHis A	Commercial vector for L-ara induced expression Cb^r	Invitrogen
Constructs		
YscU	*yscU* full length in pBADmycHis A	This study
$YscU_{K212A}$	$yscU_{K212A}$ in pBADmycHis A	This study
$YscU_{E213A}$	$yscU_{E213A}$ in pBADmycHis A	This study
$YscU_{K215A}$	$yscU_{K215A}$ in pBADmycHis A	This study
$YscU_{K218A}$	$yscU_{K218A}$ in pBADmycHis A	This study
$YscU_{E220A}$	$yscU_{E220A}$ in pBADmycHis A	This study
$YscU_{K222A}$	$yscU_{K222A}$ in pBADmycHis A	This study
$YscU_{R223A}$	$yscU_{E224A}$ in pBADmycHis A	This study
$YscU_{E224A}$	$yscU_{E224A}$ in pBADmycHis A	This study
$YscU_{K226A}$	$yscU_{K226A}$ in pBADmycHis A	This study
$YscU_{K222A/K226A}$	$yscU_{K222A/K226A}$ in pBADmycHis A	This study
$YscU^6$	$yscU^6$ (K212A, K215A, K218A, K222A, R223A and K226A) in pBADmycHis A	This study
GST-$YscU_C$	$yscU_C$ in pGEX-6p-3	(29)
GST-$YscU_C^6$	$yscU_C^6$ in pGEX-6p-3	This study
GST-$YscU_{CNK218A}$	$yscU_{CNK218A}$ in pGEX-6p-3	This study
GST-$YscU_{CNE220A}$	$yscU_{CNE220A}$ in pGEX-6p-3	This study
GST-$YscU_{CNR223A}$	$yscU_{CNR223A}$ in pGEX-6p-3	This study
GST-$YscU_{CNK222A/K226A}$	$yscU_{CNK222A/K226A}$ in pGEX-6p-3	This study

[a] Km^r, kanamycin resistance, Cb^r, carbenicillin resistance

Table S3: Primers used in this study

Primer name	Primer sequence (5'- 3')	Restriction sites
Primers for sub-cloning		
fw_pGEX_yscU$_{CN}$	cgcggatccTactatcaatatattaaggaactta	*Bam*HI
rv_pGEX_yscU$_{CN}$	tccccccggggttaattagctaccaccactgatgag	*Sma*I
Primers for site-directed mutagenesis		
fw_pBAD_yscU$_{FL}$	catgccatggtgagcggagaaaagacagag	*Nco*I
rv_yscU$_{FL}$_K212A	gctcattttaagttccgcaatatattgatagtattcaaaggc	
fw_yscU$_{FL}$_K212A	gcctttgaatactatcaatatattgcggaacttaaaatgagc	
rv_pBAD_yscU$_{FL}$	cggaattcttataacatttcggaatgttgtttc	*Eco*RI
rv_yscU$_{FL}$_E213A	gctcattttaagtgccttaatatattgatagtattcaaaggc	
fw_yscU$_{FL}$_E213A	gcctttgaatactatcaatatattaaggcacttaaaatgagc	
rv_yscU$_{FL}$_K215A	gctcattgcaagttccttaatatattgatagtattcaaaggc	
fw_yscU$_{FL}$_K215A	gcctttgaatactatcaatatattaaggaacttgcaatgagc	
rv_yscU$_{FL}$_K218A	gatctcatccgcgctcattttaagttccttaatatattgatag	
fw_yscU$_{FL}$_K218A	ctatcaatatattaaggaacttaaaatgagcgcggatgagatc	
rv_yscU$_{FL}$_E220A	ccatttctttgtactcgcgtttgatcgcatccttgctcat	
fw_yscU$_{FL}$_E220A	atgagcaaggatgcgatcaaacgcgagtacaaagaaatgg	
rv_yscU$_{FL}$_K222A	accctccatttctttgtactcgcgtgcgatctcatccttgctc	
fw_yscU$_{FL}$_K222A	gagcaaggatgagatcgcacgcgagtacaaagaaatggagggt	
rv_yscU$_{FL}$_R223A	ctccatttctttgtactcggctttgatctcatccttgctcat	
fw_yscU$_{FL}$_R223A	atgagcaaggatgagatcaaagccgagtacaaagaaatggag	
rv_yscU$_{FL}$_E224A	gctaccctccatttctttgtacgcgcgtttgatctcatcc	
fw_yscU$_{FL}$_E224A	ggatgagatcaaacgcgcgtacaaagaaatggagggtagc	
rv_yscU$_{FL}$_K226A	ctgggctaccctccatttctgcgtactcgcgtttgatctc	
fw_yscU$_{FL}$_K226A	gagatcaaacgcgagtacgcagaaatggagggtagcccag	
rv_yscU$_{FL}$_K222A/K226A	ctgggctaccctccatttctgcgtactcgcgtgcgatctc	
fw_yscU$_{FL}$_K222A/K226A	gagatcgcacgcgagtacgcagaaatggagggtagcccag	

Table S4. Selected physical chemical properties of $YscU_{CN}$ and helices 1-3 at pH 6.0 and 7.0: computed net charge, Wimley-White hydrophobicities (7) and Eisenberg hydrophobic moment (8).

pH	helix	residues	charge	hydroph[1] (w/if)	hydroph[2] (w/o)	hmoment[3]
6.0	1	211-215	1.0	3.1	6.9	2.4
	2	218-229	-0.9	11.6	25.9	3.9
	3	234-246	3.8	6.7	14.0	2.1
	$YscU_{CN}$		5.9	33.2	67.4	
7.0	1	211-215	1.0	3.1	6.9	2.4
	2	218-229	-1.0	11.6	25.9	3.9
	3	234-246	3.2	5.9	11.8	2.2
	$YscU_{CN}$		5.2	32.4	65.1	

1. ΔG for transfer from water to POPC vesicle interface (Wimley-White w/if hydrophobicities) in kcal/mol.
2. ΔG for transfer from water to octanol (Wimley-White w/o hydrophobicities) in kcal/mol.
3. Eisenberg hydrophobic moment, computed with $\Delta G_{w/if}$, in kcal/mol.

SUPPLEMENTAL FIGURES

Figure S1. Overview of NMR and computed parameters for $YscU_{CN}$ in complex with SDS micelles, summarizing residue-specific dynamic and structural properties (refer to text for detailed descriptions of individual methods). Residue properties are aligned with the primary sequence, with residues color coded according to polarity, red:Glu,Asp; blue: Lys,Arg,His. S^2_{RCI}: order parameters predicted on the basis of chemical shifts using RCI (30). S^2: order parameters from relaxation data. Prot fact: solvent protection factors computed from amide ^1H exchange rates. Empty bars indicate protection factors too large to quantify accurately. Asterisks indicate protection factors not quantified due to spectral overlap. D5S/Mn^{2+} PRE: Induced paramagnetic relaxation enhancements. $\Delta\delta$ pH: mean chemical shift response to pH 6$\rightarrow$7 perturbation. $^3J_{HNHA}$: (H^N,H^α) ^3J-coupling; filled black circles: $^3J<6Hz$; gray circles: $6Hz<{}^3J<8Hz$; empty circles: $^3J>8Hz$. $d_{mn}(i,i+j)$: ^1H-^1H dipolar couplings; for d(i,i+1) bars at residue i are proportional to NOE magnitude. Sequential $d_{\alpha N}$ have been scaled by $\times 1/2$ relative to d_{NN} and $d_{\alpha N}$. Empty bars indicate visible NOEs not quantified due to spectral overlap. Asterisks indicate NOEs not observed due to overlapping crosspeaks. For d(i,i+2-4) horizontal lines link residues involved in NOEs. $\Delta\delta^{13}C^\alpha$: difference of $^{13}C^\alpha$ shift from standard random coil value. MICS: bars indicate α-helical regions predicted from chemical shifts with program MICS (31), with regions where $S^2_{RCI}>0.7$ indicated. PSI-PRED: bars indicate predicted α-helical regions.

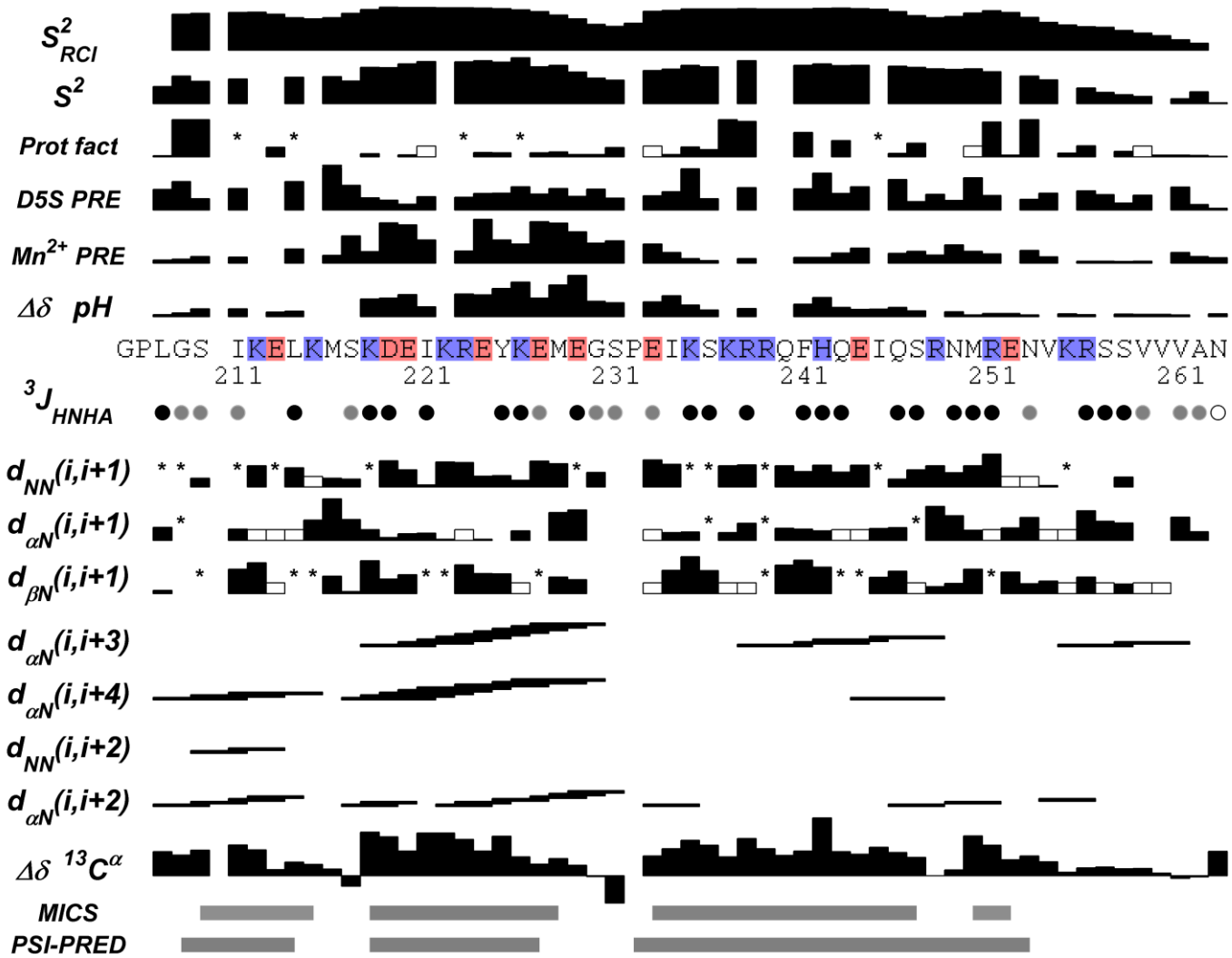
S^2_{RCI}
S^2
Prot fact
D5S PRE
Mn^{2+} PRE
$\Delta\delta$ pH
GPLGS IKELKMSKDEIKREYKEMEGSPEIKSKRRQFHQEIQSRNMRENVKRSSVVVAN
211
221
231
241
251
261
$^3J_{HNHA}$
$d_{NN}(i,i+1)$
$d_{\alpha N}(i,i+1)$
$d_{\beta N}(i,i+1)$
$d_{\alpha N}(i,i+3)$
$d_{\alpha N}(i,i+4)$
$d_{NN}(i,i+2)$
$d_{\alpha N}(i,i+2)$
$\Delta\delta\ ^{13}C^{\alpha}$
MICS
PSI-PRED

Figure S2. Relaxation data reveal global and residue-specific dynamics within the $YscU_{CN}$-SDS complex. Backbone ^{15}N NMR relaxation rates R_1 and R_2 and ^{15}N-^{1}H NOEs for $YscU_{CN}$ in complex with SDS, displayed against the primary sequence of $YscU_{CN}$.

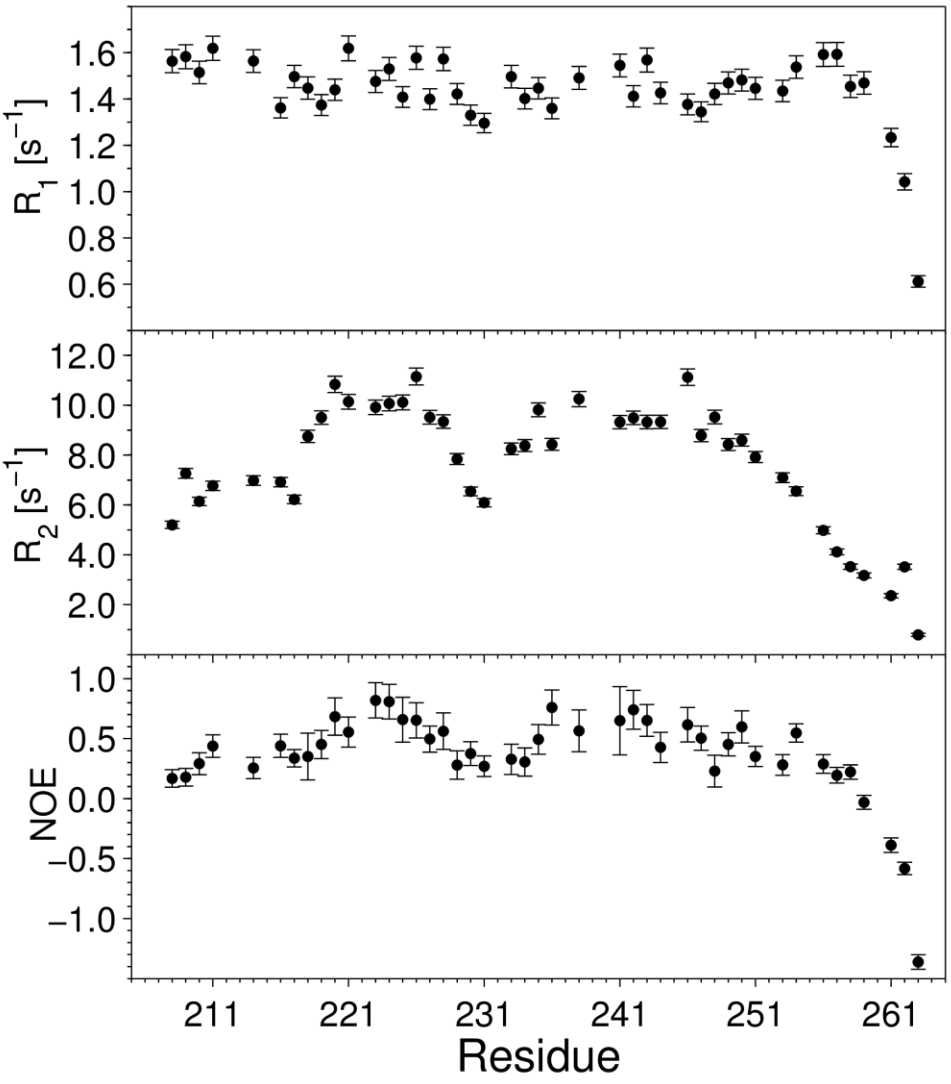

Figure S3. Residue specific chemical shift responses to a solvent pH perturbation correlate with local solvent exposure. Mean change in the backbone $^{1}H^{N}$, ^{15}N shifts in SDS-bound $YscU_{CN}$ due to an increase in pH from 6.0 to 7.0, displayed against the primary sequence of $YscU_{CN}$.

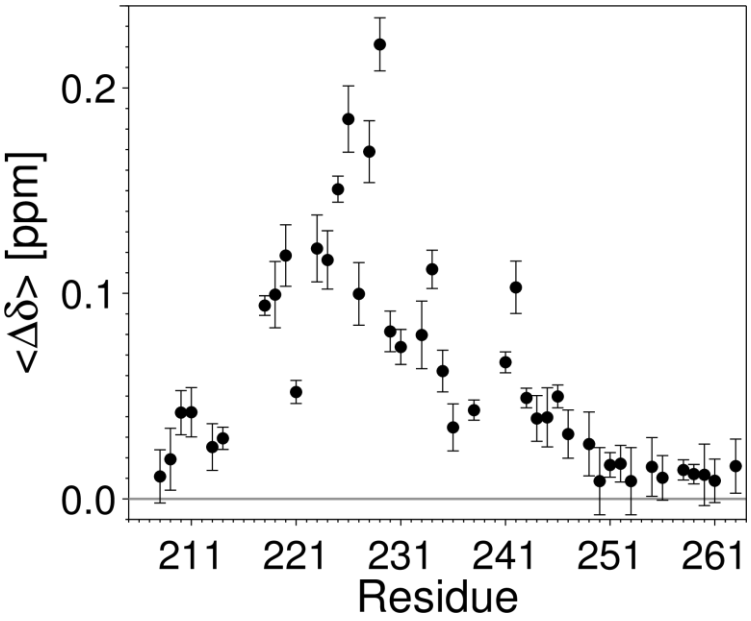

Figure S4. Solvent protection factors P_{solv} computed from backbone amide exchange rates for backbone amide H^N in SDS-bound $YscU_{CN}$, displayed against the primary sequence of $YscU_{CN}$. Small empty squares indicate residues exhibiting large but highly uncertain P_{solv} (k_{ex} below the detection limit).

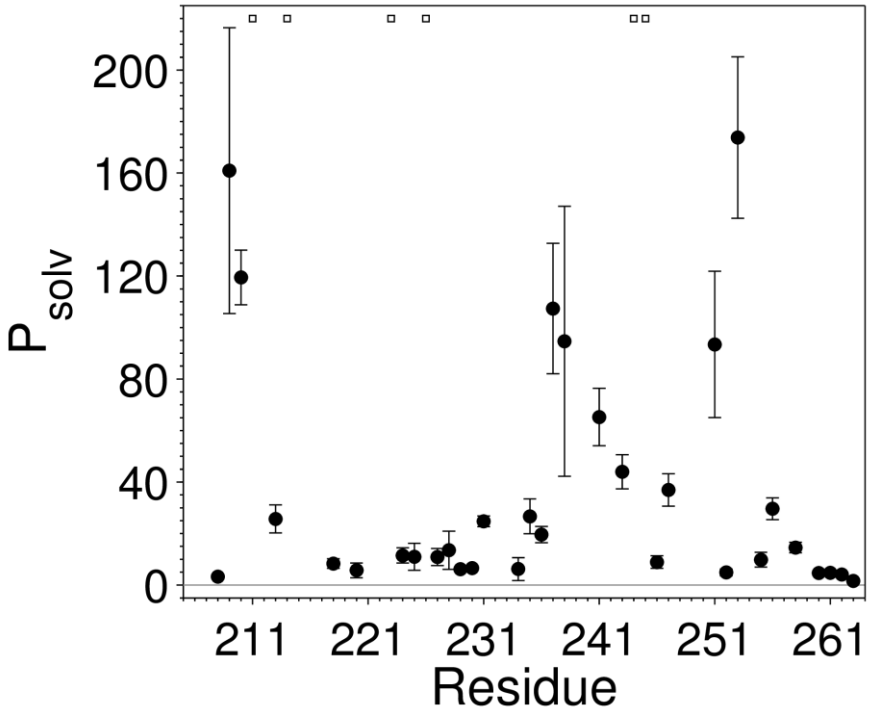

SUPPLEMENTAL REFERENCES

1. Schwieters, C. D., J. J. Kuszewski, and G. M. Clore. 2006. Using Xplor-NIH for NMR molecular structure determination. Prog Nucl Mag Res Sp 48:47-62.
2. Schwieters, C. D., J. J. Kuszewski, N. Tjandra, and G. M. Clore. 2003. The Xplor-NIH NMR molecular structure determination package. Journal of Magnetic Resonance 160:65-73.
3. Helgstrand, M., P. Kraulis, P. Allard, and T. Härd. 2000. Ansig for Windows: an interactive computer program for semiautomatic assignment of protein NMR spectra. J. Biomol. NMR 18:329-336.
4. Shen, Y., F. Delaglio, G. Cornilescu, and A. Bax. 2009. TALOS plus : a hybrid method for predicting protein backbone torsion angles from NMR chemical shifts. J Biomol NMR 44:213-223.

5. Laskowski, R. A., M. W. Macarthur, D. S. Moss, and J. M. Thornton. 1993. Procheck - a program to check the stereochemical quality of protein structures. Journal of Applied Crystallography 26:283-291.
6. Kabsch, W., and C. Sander. 1983. Dictionary of Protein Secondary Structure - Pattern-Recognition of Hydrogen-Bonded and Geometrical Features. Biopolymers 22:2577-2637.
7. White, S. H., and W. C. Wimley. 1998. Hydrophobic interactions of peptides with membrane interfaces. Biochim Biophys Acta 1376:339-352.
8. Eisenberg, D., R. M. Weiss, and T. C. Terwilliger. 1984. The Hydrophobic Moment Detects Periodicity in Protein Hydrophobicity. P Natl Acad Sci-Biol 81:140-144.
9. Kay, L. E., D. A. Torchia, and A. Bax. 1989. Backbone Dynamics of Proteins as Studied by N-15 Inverse Detected Heteronuclear Nmr-Spectroscopy - Application to Staphylococcal Nuclease. Biochemistry 28:8972-8979.
10. Hwang, T. L., P. C. van Zijl, and S. Mori. 1998. Accurate quantitation of water-amide proton exchange rates using the phase-modulated CLEAN chemical EXchange (CLEANEX-PM) approach with a Fast-HSQC (FHSQC) detection scheme. J Biomol NMR 11:221-226.
11. Mori, S., C. Abeygunawardana, M. O. Johnson, and P. C. van Zijl. 1995. Improved sensitivity of HSQC spectra of exchanging protons at short interscan delays using a new fast HSQC (FHSQC) detection scheme that avoids water saturation. J Magn Reson B 108:94-98.
12. Bai, Y., J. S. Milne, L. Mayne, and S. W. Englander. 1993. Primary structure effects on peptide group hydrogen exchange. Proteins: Struct. Funct. Genet. 17:75-86.
13. Connelly, G. P., Y. W. Bai, M. F. Jeng, and S. W. Englander. 1993. Isotope effects in peptide group hydrogen-exchange. Proteins: Struct. Funct. and Genet. 17:87-92.
14. Markley, J. L., A. Bax, Y. Arata, C. W. Hilbers, R. Kaptein, B. D. Sykes, P. E. Wright, and K. Wuthrich. 1998. Recommendations for the presentation of NMR structures of proteins and Nucleic Acids (Reprinted from Pure and Applied Chemistry, vol 70, pgs 117-142, 1998). J Mol Biol 280:933-952.
15. Buchan, D. W., S. M. Ward, A. E. Lobley, T. C. Nugent, K. Bryson, and D. T. Jones. 2010. Protein annotation and modelling servers at University College London. Nucleic Acids Res 38:W563-W568.
16. Jones, D. T. 1999. Protein secondary structure prediction based on position-specific scoring matrices. J Mol Biol 292:195-202.
17. Mandel, A. M., M. Akke, and A. G. Palmer. 1995. Backbone Dynamics of Escherichia-Coli Ribonuclease Hi - Correlations with Structure and Function in an Active Enzyme. J Mol Biol 246:144-163.
18. Fushman, D., S. Cahill, and D. Cowburn. 1997. The main-chain dynamics of the dynamin pleckstrin homology (PH) domain in solution: Analysis of N-15 relaxation with monomer/dimer equilibration. J Mol Biol 266:173-194.
19. Hall, J. B., and D. Fushman. 2003. Characterization of the overall and local dynamics of a protein with intermediate rotational anisotropy: Differentiating

between conformational exchange and anisotropic diffusion in the B3 domain of protein G. J Biomol NMR 27:261-275.
20. Wennerst.H. 1972. Nuclear Magnetic-Relaxation Induced by Chemical Exchange. Mol Phys 24:69-80.
21. Lipari, G., and A. Szabo. 1982. Model-Free Approach to the Interpretation of Nuclear Magnetic-Resonance Relaxation in Macromolecules .1. Theory and Range of Validity. J. Am. Chem. Soc. 104:4546-4559.
22. Lipari, G., and A. Szabo. 1982. Model-Free Approach to the Interpretation of Nuclear Magnetic-Resonance Relaxation in Macromolecules .2. Analysis of Experimental Results. J Am Chem Soc 104:4559-4570.
23. Clore, G. M., A. Szabo, A. Bax, L. E. Kay, P. C. Driscoll, and A. M. Gronenborn. 1990. Deviations from the Simple 2-Parameter Model-Free Approach to the Interpretation of N-15 Nuclear Magnetic-Relaxation of Proteins. J Am Chem Soc 112:4989-4991.
24. Ortega, A., and J. G. de la Torre. 2003. Hydrodynamic properties of rodlike and disklike particles in dilute solution. J Chem Phys 119:9914-9919.
25. Sheftic, S. R., R. L. Croke, J. R. LaRochelle, and A. T. Atexandrescu. 2009. Electrostatic Contributions to the Stabilities of Native Proteins and Amyloid Complexes. Methods in Enzymology, Vol 466: Biothermodynamics, Pt B 466:233-+.
26. Ma, K., E. L. Clancy, Y. B. Zhang, D. G. Ray, K. Wollenberg, and M. G. Zagorski. 1999. Residue-specific pK(a) measurements of the beta-peptide and mechanism of pH-induced amyloid formation. J Am Chem Soc 121:8698-8706.
27. Studier, F. W., and B. A. Moffatt. 1986. Use of Bacteriophage-T7 Rna-Polymerase to Direct Selective High-Level Expression of Cloned Genes. J. Mol. Biol. 189:113-130.
28. Lavander, M., L. Sundberg, P. J. Edqvist, S. A. Lloyd, H. Wolf-Watz, and A. Forsberg. 2002. Proteolytic cleavage of the FlhB homologue YscU of Yersinia pseudotuberculosis is essential for bacterial survival but not for type III secretion. J Bacteriol 184:4500-4509.
29. Frost, S., O. Ho, F. H. Login, C. F. Weise, H. Wolf-Watz, and M. Wolf-Watz. 2012. Autoproteolysis and intramolecular dissociation of Yersinia YscU precedes secretion of its C-terminal polypeptide YscU(CC). Plos One 7:e49349.
30. Berjanskii, M. V., and D. S. Wishart. 2007. The RCI server: rapid and accurate calculation of protein flexibility using chemical shifts. Nucleic Acids Res 35:W531-W537.
31. Shen, Y., and A. Bax. 2012. Identification of helix capping and b-turn motifs from NMR chemical shifts. J Biomol NMR 52:211-232.